J. Fluid Mech. (2010), *vol.* 660, *pp.* 258–281. © Cambridge University Press 2010
doi:10.1017/S0022112010002697

Particle focusing in a suspension flow through a corrugated tube

G. F. HEWITT AND J. S. MARSHALL†
School of Engineering, University of Vermont, Burlington, VT 05405, USA

(Received 19 August 2009; revised 3 May 2010; accepted 5 May 2010;
first published online 21 July 2010)

A computational study is performed of the transport of a particulate suspension through a corrugated tube using a discrete-element method (DEM). The tube is axisymmetric with a radius that varies sinusoidally along the tube length, which, in the presence of a mean suspension flow, leads to periodic inward and outward acceleration of the advected particles. The oscillations in radial acceleration and straining rate lead to a net radial drift, with mean acceleration measuring about an order of magnitude smaller than the instantaneous radial acceleration, which over time focuses small particles within the tube. The foundations of particle focusing in this flow are examined analytically using lubrication theory, together with a low-Stokes-number approximation for the particle drift. This lubrication-theory solution provides the basic scaling for how the particle drift will vary with wave amplitude and wavelength. Computations are then performed using a finite-volume method for a fluid flow in the tube at higher Reynolds numbers over a range of amplitudes, wavelengths and Reynolds numbers, examining the effect of each of these variables on the averaged radial fluid acceleration. A DEM is used to simulate particle behaviour at finite Stokes numbers, and the results are compared to an asymptotic approximation valid for low Stokes numbers. At low tube Reynolds number (e.g. $Re = 10$), the drift velocity induced by the tube corrugations focuses the particles onto the tube centreline, in accordance with the low-Stokes-number approximation based on the axial-averaged fluid radial acceleration. At higher tube Reynolds numbers (e.g. $Re = 100$), the correlation between the particle radial oscillation and the fluid acceleration field leads the outermost particles to drift into a ring at a finite radius from the tube centre, with little net motion of the particles in the innermost part of the tube. At larger Stokes numbers, particles can be dispersed to the outer regions of the tube due to particle outward dispersion from the large instantaneous radial acceleration. The effects of eddy formation within the corrugation crests on particle focusing are also examined.

Key words: particle/fluid flows, suspensions

1. Introduction

Corrugated tubes and channel flows are commonly used for enhancement of fluid mixing and heat and mass transfer in laminar-flow fields. Extensive studies have been performed to examine flow regimes, fluid mixing and heat-transfer enhancement for a flow in two-dimensional symmetric corrugated channels (Nishimura *et al.*

---

† Email address for correspondence: jeffm@cems.uvm.edu

1990; Guzmán & Amon 1994, 1996; Rush, Newell & Jacobi 1999; Kim 2001; Nieno & Nobile 2001; Mahmud, Islam & Mamun 2002; Oviedo-Tolentino *et al.* 2008), axisymmetric corrugated tubes (Savvides & Gerrard 1984) and two-dimensional antisymmetric corrugated channels (Asako & Faghri 1987; Gschwind, Regele & Kottke 1995; Rush *et al.* 1999; Vasudeviah & Balamurugan 2001; Gradeck, Hoareau & Lebouché 2005). For low Reynolds numbers or sufficiently small wall slope, the flow remains attached and the straining rate on a fluid element oscillates as it is advected along the channel (Vasudeviah & Balamurugan 2001). At higher Reynolds number and/or higher wall slope, a recirculating separated region exists within the crest of each corrugation wave (Mahmud *et al.* 2002). As the flow rate is varied, these separated regions display a rich array of flow regimes, starting with a steady-flow condition and passing through periodic, quasi-periodic and finally chaotic states as the Reynolds number is increased (Amon, Guzmán & Morel 1996; Guzmán & Amon 1994, 1996). The ability of the oscillatory inlet flow rate to induce vortex shedding and enhanced mixing is reported for both two-dimensional symmetric corrugated channels (Sobey 1980; Stephanoff, Sobey & Bellhouse 1980; Nishimura *et al.* 1989; Nishimura & Kawamura 1995) and axisymmetric corrugated tubes (Ralph 1986; Lee, Kang & Lim 1999). Conditions for instability of corrugated channel flows have been reported in both theoretical and experimental/computational studies (Cho, Kim & Shin 1998; Selvarajan, Tulapurkara & Ram 1999; Cabal, Szumbarski & Floryan 2002; Asai & Floryan 2006). Instability of a particle-laden suspension flow in a wavy-walled channel is examined by Usha, Senthilkumar & Tulapurkara (2005) using a two-phase continuum theory; however, this paper does not consider particle migration in the channel.

Many applications of corrugated tubes or channel flows involve transport of a two-phase aerosol or aqueous suspension. For instance, aerosol transport of dust through a radiator channel can sometimes lead cooling system fouling for construction machinery working in dusty environments. A common application of corrugated tubes is collapsible plastic or metallic ducts, which are used, for instance, for dryer ventilation lines and are prone to increased resistance and clogging due to dust deposition. There are several biological applications involving passage of aqueous particle or cell suspensions through corrugated tubes, e.g. in transport of the intestinal fluid (chyme) through the colon, which is formed of periodic ‘haustral pockets’ positioned along its length (Putz & Pabst 2000). Other cases involving a particle suspension flow in channels and tubes occur in algae production in tubular bioreactors (Christi 2007; Sastre *et al.* 2007) and micro-fluidic particle and cell cytometry systems (Ormerod 1999).

Particle inertial focusing refers to the hydrodynamic-induced drift of particles to certain preferential locations of a micro-channel flow in a manner that is dependent on the particle inertia. Di Carlo *et al.* (2007) report the presence of a continuous inertial focusing of 1–10 μm diameter particles in a suspension flowing through a stationary antisymmetric corrugated micro-channel with repeated S-shaped curves to form a continuous undulating waveform. Choi *et al.* (2008) and Choi & Park (2008) present a hydrodynamic focusing method based on the flow response and the resulting particle drift induced by a series of obstacles forming V-shaped patterns along different walls of the micro-channel. Other hydrodynamic focusing methods based on the flow response to an array of obstacles placed in the micro-channel have been proposed by Huang *et al.* (2004) and Davis *et al.* (2006). In all these hydrodynamic focusing systems, the particles are exposed to an alternating series of positive and negative straining as they pass by each obstacle.

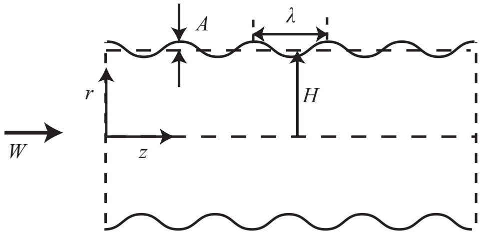

FIGURE 1. Schematic of the corrugated tube flow, showing the mean tube radius H, wave amplitude A and wavelength $\lambda = 2\pi/k$.

Recently, Marshall (2009*a*) showed that a hydrodynamic focusing (or clustering) can be induced when particles are exposed to an oscillating straining field (in the particle frame), causing particles to drift towards the nodal points of the straining field. By using the low-Stokes-number approximation for fluid drift velocity proposed by Ferry & Balachandar (2003), which yields the result that the particle drift is proportional to the negative of the fluid acceleration, this oscillatory clustering phenomenon can be related to the non-zero time average of the fluid convective acceleration. A theoretical formulation for this phenomenon was presented, which reduces the particle motion in the oscillating straining field to a damped Mathieu equation, and which subsequently predicts both the particle drift rate and the stability limitations on clustering. The method was applied to examine particle drift in a peristaltic channel flow, in which case particles drift towards the nodal points of a standing peristaltic wave.

The current study seeks to understand the implications of the oscillatory clustering mechanism for problems involving a particulate suspension flow through an axisymmetric corrugated tube. The tube corrugations induce an oscillatory straining on particles advected through the tube, centred on the tube axis. The oscillatory clustering theory of Marshall (2009*a*) would therefore suggest that the particles will drift towards the tube axis. The current paper demonstrates that indeed particles do drift towards the tube axis at low flow Reynolds numbers, but at higher flow Reynolds numbers, the rate of oscillatory clustering within the central part of the tube is greatly reduced, in part due to the effects of flow separation within the furrow regions.

The problem of particle drift in a lubrication flow through a corrugated tube is examined analytically in § 2 using an approximation of low particle Stokes number. While this analysis is highly simplified, it illustrates the basic mechanism underlying the particle-focusing phenomenon and provides a scaling for the rate of focusing in the optimal case. The computational method used for cases with larger Reynolds and Stokes numbers is described in § 3. Particle focusing at moderate flow Reynolds number ($Re_F = 10$) is examined in § 4 for a range of corrugation-wave amplitudes and wavelengths. Ring formation of particles at higher flow Reynolds number ($Re_F = 100$) is discussed in § 5. Conclusions are given in § 6.

2. Collisionless particle transport at low tube Reynolds and Stokes numbers

We consider an axisymmetric incompressible flow with velocity $\boldsymbol{u} = u(r, z)\boldsymbol{e}_r + w(r, z)\boldsymbol{e}_z$ in a corrugated tube with radius $h(z) = H + A\cos(kz)$. A schematic of the corrugated tube flow is shown in figure 1, showing the nominal tube radius H, the wave amplitude A, the wavelength $\lambda = 2\pi/k$ and the mean axial velocity W. At small flow Reynolds number ($Re_F \equiv \rho W H/\mu \ll 1$) and small slope ($kA \ll 1$), lubrication theory can be used to approximate the governing equations for the flow as

$$\frac{1}{r}\frac{\partial}{\partial r}(ru) + \frac{\partial w}{\partial z} = 0, \quad 0 = \gamma(z) + \frac{\mu}{r}\frac{\partial}{\partial r}\left(r\frac{\partial w}{\partial r}\right), \tag{2.1}$$

where $\gamma(z) \equiv \partial p/\partial z$, and ρ and μ are the fluid density and viscosity, respectively. In (2.1), the flow Reynolds number is assumed to be sufficiently small that the pressure gradient is balanced by the viscous shear term, and the fluid inertia is negligible. Integration of (2.1) yields a solution for the velocity components as

$$w(r,z) = -\frac{\gamma(z)}{4\mu}[h^2(z) - r^2], \tag{2.2a}$$

$$u(r,z) = \frac{\gamma(z)r}{4\mu}h\frac{\mathrm{d}h}{\mathrm{d}z} + \frac{r}{16\mu}(2h^2 - r^2)\frac{\mathrm{d}\gamma}{\mathrm{d}z}. \tag{2.2b}$$

Applying the no-slip condition at $r = h(z)$, (2.2b) yields the restriction

$$h^4\gamma = C, \tag{2.3}$$

where C is a constant of integration. The average velocity over a cross-section of the tube is obtained using (2.1) and (2.3) as

$$W_C(z) \equiv \frac{2}{h^2}\int_0^{h(z)} w(r,z) r\,\mathrm{d}r = -\frac{C}{8\mu\, h^2(z)}. \tag{2.4}$$

A nominal axial velocity is defined by $W \equiv -C/8\mu H^2$. Non-dimensionalizing u and w by W and non-dimensionalizing r, h and z by H yields the dimensionless velocity field as

$$w' = \frac{2}{h'^2}[1 - (r'/h')^2], \quad u' = -\frac{2r'\alpha\eta}{h'^3}[1 - (r'/h')^2]\sin(\alpha z'), \tag{2.5}$$

where $\alpha \equiv kH$, $\eta \equiv A/H$ and a prime denotes a dimensionless variable. From these definitions, we note that the product $\alpha\eta = Ak$, which is the scaling for the maximum slope of the corrugation wave.

A simplified form of the particle momentum equation that balances particle inertia with the Stokes drag for neutrally buoyant particles is given by

$$\frac{\mathrm{d}\boldsymbol{v}'}{\mathrm{d}t'} = -\frac{1}{St}(\boldsymbol{v}' - \boldsymbol{u}'), \tag{2.6}$$

where $\boldsymbol{v}'$ and $\boldsymbol{u}'$ are the dimensionless particle velocity and fluid velocity at the particle centroid location, respectively, and St is the particle Stokes number. The Stokes number is related to the flow Reynolds number and the dimensionless particle diameter $\varepsilon = d/H$ by

$$St = \varepsilon^2 Re_F/18\chi, \tag{2.7}$$

where $\chi \equiv \rho/\rho_P$ is the ratio of the fluid to particle density ($\chi = 1$ for the neutrally buoyant particles used in the current paper). Even though both the particle Reynolds number and the Stokes number are assumed to be small, the fact that there are only two terms in (2.6) implies that the particle inertia will always remain of the same order of magnitude as the particle drag term, such that as the Stokes number approaches zero, the particle velocity will approach that of the surrounding fluid flow. For flows with low Stokes number, the so-called fast Euler approximation (Ferry & Balachandar 2003) can be employed, in which the particle acceleration $\mathrm{d}\boldsymbol{v}/\mathrm{d}t$ is approximated by the fluid material derivative $\mathrm{D}\boldsymbol{u}/\mathrm{D}t = \partial \boldsymbol{u}/\partial t + (\boldsymbol{u} \cdot \nabla)\boldsymbol{u}$. Under this approximation, (2.6) can be rearranged to write

$$\boldsymbol{v}' = \boldsymbol{u}' - St\frac{\mathrm{D}\boldsymbol{u}'}{\mathrm{D}t'} + O(St^2). \tag{2.8}$$

The dimensionless particle drift velocity $\boldsymbol{u}'_D$ is given by (2.8) to leading order in St as $\boldsymbol{u}'_D = -St\,\boldsymbol{a}'$, where $\boldsymbol{a}' = \mathrm{D}\boldsymbol{u}'/\mathrm{D}t'$ is the dimensionless fluid acceleration at the instantaneous particle centroid location.

The radial position of each particle oscillates as the particle travels in the axial direction over a distance of one furrow wavelength λ. We define $\bar{r}_n$ as the average radial position of particle n as it passes through a furrow, or

$$\bar{r}_n(z_n) = \frac{1}{\lambda}\int_{z_n-\lambda}^{z_n} r_n(z)\,\mathrm{d}z, \tag{2.9}$$

where (r_n, z_n) denote the instantaneous radial and axial coordinates of particle n. Variables averaged in accordance with (2.9) are henceforth referred to as furrow-averaged quantities. Since z_n is a function of time, the furrow-averaged radial position can also be written as a function of time $\bar{r}_n(t)$, the rate of change of which represents the radial particle drift.

In the case that the tube corrugation amplitude is small, such that $\eta \ll 1$, the acceleration $\boldsymbol{a}$ of the fluid at the particle centroid can be expanded in a Taylor series about the furrow-averaged position $\bar{r}_n(t)$, such that

$$\boldsymbol{a}'(r'_n) = \boldsymbol{a}'(\bar{r}'_n) + (r'_n - \bar{r}'_n)\frac{\partial \boldsymbol{a}'}{\partial r'}\,|_{r=\bar{r}_n} + \cdots, \tag{2.10}$$

where the omitted terms are of higher order in the small parameter η than the two retained terms. We define the first and second particle drift velocities, $\boldsymbol{u}'_{D1}$ and $\boldsymbol{u}'_{D2}$, as the furrow-averaged particle velocities generated by the each of the terms on the right-hand side of (2.10), respectively, such that

$$\boldsymbol{u}'_{D1} = -St\,\overline{\boldsymbol{a}'(\bar{r}')}, \quad \boldsymbol{u}'_{D2} = -St\,[\overline{(r' - \bar{r}')\partial \boldsymbol{a}'/\partial r'}]. \tag{2.11}$$

The first drift velocity is simply the average of the fluid acceleration along the tube at the furrow-averaged radial position of the particle. The second drift velocity is related to the correlation between the radial oscillation of the particle about the furrow-averaged location and the variation of the radial-acceleration gradient. These two terms of the Taylor series are found to scale similarly with the Stokes number and the product $\alpha\eta$.

In a steady flow, the definition of a streamline can be integrated to write $r' - \bar{r}' = \int (u'/w')\,\mathrm{d}z'$. Substituting the dimensionless velocity field (2.5) into the fluid material derivative and averaging over the tube perturbation wavelength yields the first and second fluid radial drift velocities for the lubrication theory to leading order in η as

$$u'_{D1} = -2St(\alpha\eta)^2\bar{r}'(1 - \bar{r}'^2)(3 - 7\bar{r}'^2), \tag{2.12a}$$

$$u'_{D2} = 2St(\alpha\eta)^2\bar{r}'(1 - \bar{r}'^2)(1 - 5\bar{r}'^2). \tag{2.12b}$$

Details of the derivation of (2.12*a*,*b*) are given in the Appendix. The first drift velocity is negative (inward drift) for particles in the region $0 < r' < \sqrt{3/7}$ and positive (outward drift) for $\sqrt{3/7} < r' < 1$. The second drift velocity is positive for $0 < r' < 1/\sqrt{5}$ and negative for $1/\sqrt{5} < r' < 1$.

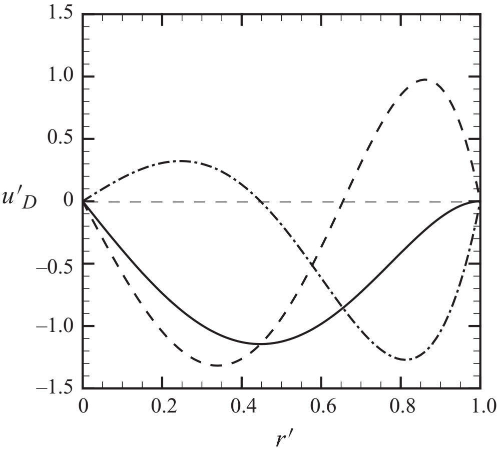

FIGURE 2. Plot showing first particle drift velocity u'_{D1} (dashed line), second particle drift velocity u'_{D2} (dashed–dotted line) and net particle drift velocity $u'_D = u'_{D1} + u'_{D2}$ (solid line) for low-Stokes-number particle transport in a tube given by the lubrication theory. All velocities are normalized by $St\,(\alpha\eta)^2$.

The net particle drift velocity u'_D is given by the sum of u'_{D1} and u'_{D2}, which is normalized by $St\,(Ak)^2$ and plotted in figure 2 as a function of radius. Within the central part of the tube ($r' < 0.4$), the magnitude of the first drift velocity is significantly greater than that of the second drift velocity, and the direction of the two velocities is opposite to each other. Each of the drift velocities change sign within the outer part of the tube, and the magnitudes of the two drift velocities in this region are similar. The net effect is to keep the total drift velocity negative throughout the tube, implying that under the lubrication theory all particles will drift towards the tube centre at a velocity that is proportional to $St(Ak)^2$. The maximum particle drift velocity occurs at approximately $r' \cong 0.45$, for which

$$u'_{D,max} \cong -1.14\,St(kA)^2. \tag{2.13}$$

3. Computational method

For cases at finite Reynolds and Stokes numbers, the flow and particle transport is computed using an axisymmetric finite-volume method for the fluid and a three-dimensional discrete-element method (DEM) for the particles. Computations are performed with neutrally buoyant particles having small concentrations (less than 0.5 %) and small particle mass loading; so two-way phase interactions can be neglected (Crowe, Sommerfeld & Tsuji 1998). Throughout the remainder of this paper, all numerical values of variables are non-dimensionalized using the nominal axial velocity W and the nominal tube radius H for velocity and length scales, respectively. Below we discuss the computational methods used for the fluid and particles separately, including some examples of the flow structure in the tube.

3.1. *Fluid-flow computational method and example results*

Computations of the flow of an incompressible fluid in an axisymmetric corrugated tube are performed using a finite-volume method with a block-structured grid (Lai 2000). The numerical method stores all dependent variables at the cell centres of a

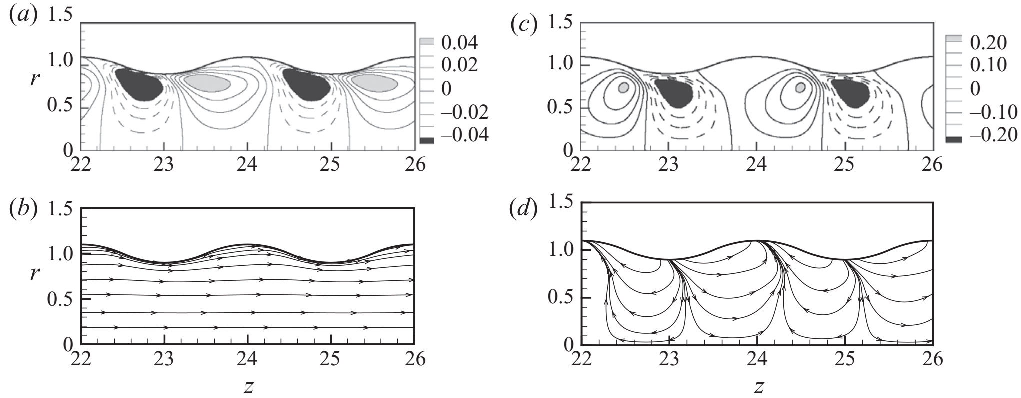

FIGURE 3. Contours of (*a*) radial velocity and (*c*) negative fluid acceleration for a case with $A = 0.1$, $\lambda = 2$ and $Re_F = 100$, which exhibits no flow recirculation. Dashed lines indicate negative contour values and solid lines indicate positive contour values. Streamlines are shown for (*b*) fluid velocity and (*d*) negative fluid acceleration.

structured grid in the *r*–*z* plane, and uses a novel interpolation method to yield a second-order accurate spatial approximation of the diffusive and convective fluxes on the cell boundaries for arbitrary meshes. The PISO algorithm (pressure implicit with splitting of operators; Issa 1985) is used to couple momentum and continuity equations. Numerical stability is enhanced by weighting the time derivative between second-order and first-order upwind approximations, with characteristically about 90–10 weighting ratio. The flow is periodic over an axial distance of 10 times the nominal tube radius. The time step in all fluid-flow computations is held fixed at $\Delta t = 0.01$.

Cases exploring corrugation-wave amplitudes ranging from 0.1 to 0.5 and wavelengths of 1–10 were examined with flow Reynolds numbers (Re_F) of both 10 and 100. Each fluid run was iterated until the pressure and velocity residuals reached values of about 10^{-8}. Several of the large-amplitude cases with $Re_F = 100$ exhibit recirculating flows within the tube corrugations, which reduces the magnitude of oscillating straining experienced by the advected particles. All of the $Re_F = 10$ cases exhibit no recirculation. Contours and streamlines of the radial velocity are shown in figures 3(*a*) and 3(*b*) for a case with $A = 0.1$, $\lambda = 2$ and $Re_F = 100$. This particular flow does not exhibit a recirculation eddy in the wave peaks, but instead the flow remains attached everywhere within the tube. The flow is typified by alternating regions of outward and inward flow along the tube length. The transition between the outward and inward flow results in a region of large outward-oriented acceleration just under the wave trough, as seen in the contour plot and streamline plot of the negative acceleration field in figures 3(*c*) and 3(*d*). According to the drift velocity result (2.8), which is valid for low Stokes numbers, the dimensionless negative acceleration field is equal to the ratio of the dimensionless particle drift velocity divided by the Stokes number; so the streamlines of negative acceleration are coincident with the streamlines of the particle drift velocity. Consequently, this region of a large outward radial acceleration under the wave trough corresponds to a region of a large inward-directed particle drift. A weaker outward particle drift occurs downstream of the wave crest, just upstream of the region of the inward radial flow.

The effect of recirculation within the tube is examined for a case with $A = 0.2$, $\lambda = 2$ and $Re_F = 100$. The radial-velocity contours and streamlines are shown in figures 4(*a*)

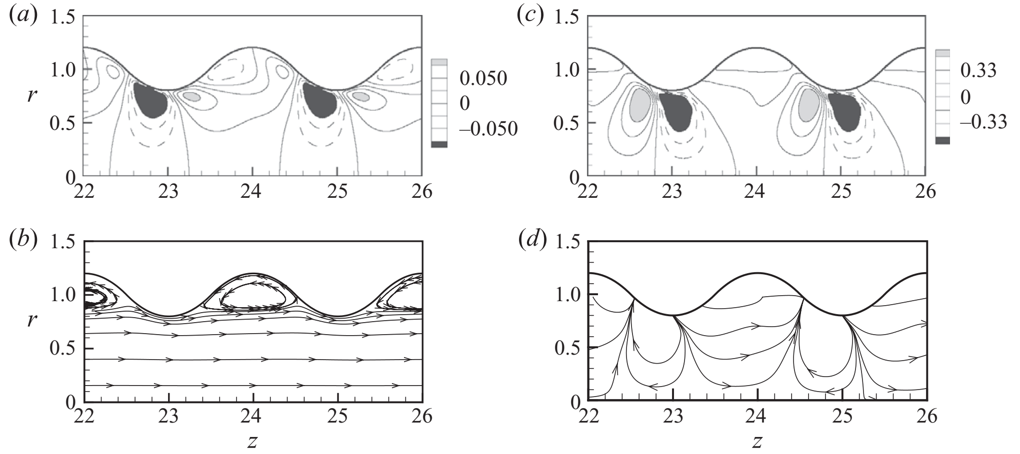

FIGURE 4. Contours of (*a*) radial velocity and (*c*) negative fluid acceleration for a case with $A = 0.2$, $\lambda = 2$ and $Re_F = 100$, exhibiting recirculation within the outer parts of the tube. Dashed lines indicate negative contour values and solid lines indicate positive contour values. Streamlines are shown for (*b*) fluid velocity and (*d*) negative acceleration.

and 4(*b*). This flow exhibits a recirculation in the furrows of the channel, as most easily observed in the streamline plot in figure 4(*b*), although the velocity magnitude within this recirculating region is very low. The larger value of the wave amplitude results in higher magnitude of the radial-velocity component and radial acceleration compared to the $A = 0.1$ case. While there are regions of both inward and outward particle drift, the regions of the inward particle drift have larger magnitude than those of the outward drift, as was also observed for the case with no recirculating flow.

Grid independence of the fluid-flow computations is examined by comparing the radial acceleration averaged across the tube length. Though quantities such as velocity converge with a relatively coarse grid, quantities that are averaged along the tube axis (such as the axially averaged acceleration, which is used in the first particle drift velocity) require a much finer grid to achieve convergence. In part, this difference is due to the fact that the average fluid acceleration is about two orders of magnitude smaller than the instantaneous acceleration. A representative grid geometry of amplitude $A = 0.1$ and wavelength $\lambda = 2$, with a Reynolds number of 100, was utilized for the grid sensitivity study. The sensitivity study examined the effect of grid density on the average acceleration values using five different grids, labelled grid A (1200×50 points), grid B (1800×100 points), grid C (2400×150 points), grid D (3000×200 points) and grid E (4050×300 points), all over a domain covering the region $0 \leqslant r \leqslant 1.1$ and $0 \leqslant z \leqslant 10$. A plot of the average radial acceleration for these five grids is shown in figure 5. The peak value of the average acceleration for grid D was found to be within 1.3 % of that for the most refined grid E. All of the computations in the paper are performed using grid resolution similar to that in grid D.

As a further check on numerical error, the average radial velocity along each axial line of the grid is computed. Theoretically, the axially averaged radial velocity should be zero in a periodic flow field. While the computed average radial velocity is small (less than 0.2 % of the peak radial-velocity values), the drift induced by non-zero average radial velocity is comparable to the estimated particle radial drift given by (2.8), since both the fluid axially averaged radial acceleration and the Stokes numbers are small. Potential errors induced by the non-zero average radial velocity

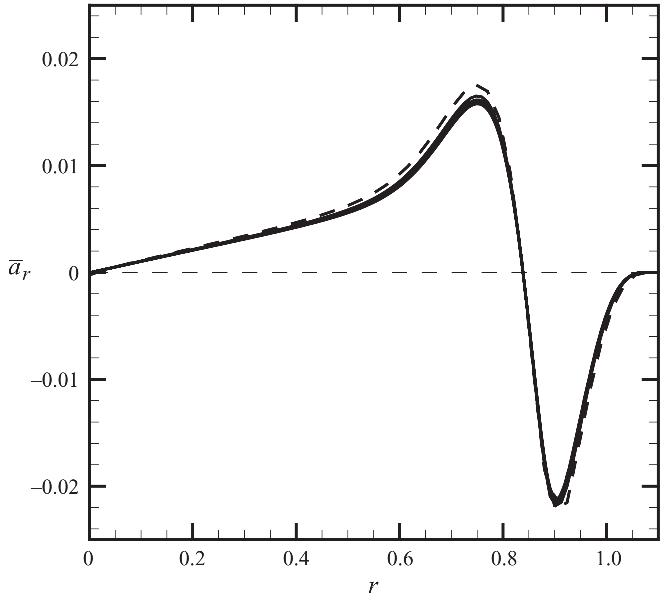

FIGURE 5. Grid sensitivity study showing the axially averaged radial acceleration across the interrogation region as a function of radius for grids A–E. The coarsest grid (grid A) is indicated using a dashed line.

are corrected by subtracting the axially averaged radial velocity from the local radial velocity at each grid point. Computations performed both with and without this correction are found to exhibit no discernable difference for the $Re_F = 10$ case, but there are some slight differences for the $Re_F = 100$ case due to the very small average radial accelerations near the tube centre.

3.2. *Discrete-element method for particle transport*

A DEM is used to examine particle transport in a corrugated tube at finite Stokes number. The DEM has been presented in several previous papers (Marshall 2006, 2007, 2009*b*), and so only a very brief description is given here. The computational method uses a multiple time step algorithm, in which the fluid time step $\Delta t = O(H/W)$, the particle time step $\Delta t_p = O(d/W)$ and the collision time step $\Delta t_c = O(d(\rho_p^2/E_p^2 W)^{1/5})$ satisfy $\Delta t > \Delta t_p > \Delta t_c$. Here d is the particle diameter, ρ_p is the particle density and E_p is the particle elastic modulus. The method follows the motion of individual particles in the three-dimensional fluid flow by solution of the particle momentum and angular momentum equations

$$m\frac{\mathrm{d}\boldsymbol{v}}{\mathrm{d}t} = \boldsymbol{F}_F + \boldsymbol{F}_A, \quad I\frac{\mathrm{d}\boldsymbol{\Omega}}{\mathrm{d}t} = \boldsymbol{M}_F + \boldsymbol{M}_A, \tag{3.1}$$

under forces and torques induced by the fluid flow ($\boldsymbol{F}_F$ and $\boldsymbol{M}_F$) and by the particle collision ($\boldsymbol{F}_A$ and $\boldsymbol{M}_A$). In these equations, m is the particle mass and I is the moment of inertia. The dominant fluid force is the drag force, approximated by a modified form of the Stokes drag law

$$\boldsymbol{F}_d = -3\pi d\mu(\boldsymbol{v} - \boldsymbol{u}) f, \tag{3.2}$$

where $\boldsymbol{v}$ and $\boldsymbol{u}$ are the particle and local fluid velocities and f is a friction factor that accounts for the effect of local particle crowding, which takes on the value $f = 1$ for an isolated sphere. We use a correlation of Di Felice (1994) for f as a function of the local particle concentration c and the particle Reynolds number $Re_p = |\boldsymbol{v} - \boldsymbol{u}|d/\nu$. The associated fluid torque arises from a difference in the rotation rate of the particle and the local fluid region and is given by

$$\boldsymbol{M}_F = -\pi \mu d^3 \left(\boldsymbol{\Omega} - \tfrac{1}{2}\boldsymbol{\omega}\right), \tag{3.3}$$

where $\boldsymbol{\Omega}$ is the particle rotation rate and $\boldsymbol{\omega}$ is the local fluid vorticity vector. In addition to the drag force, the fluid-induced forces also include the lift force (Saffman 1965, 1968), the Magnus force (Rubinow & Keller 1961) and the added-mass and pressure-gradient forces.

Particle collisions are simulated by employing a soft-sphere collision model, where each collision includes a normal force F_n along the line of collision and frictional resistances for sliding and twisting motions of the particles, such that for a particle of radius r_i, we can write

$$\boldsymbol{F}_A = F_n \boldsymbol{n} + F_s \boldsymbol{t}_S, \quad \boldsymbol{M}_A = r_i F_s (\boldsymbol{n} \times \boldsymbol{t}_S) + M_t \boldsymbol{n}. \tag{3.4}$$

The normal vector $\boldsymbol{n}$ is written in terms of the centroids $\boldsymbol{x}_i$ and $\boldsymbol{x}_j$ of two colliding particles as

$$\boldsymbol{n} = (\boldsymbol{x}_j - \boldsymbol{x}_i)/|\boldsymbol{x}_j - \boldsymbol{x}_i|. \tag{3.5}$$

The unit vector $\boldsymbol{t}_S \equiv \boldsymbol{v}_S/|\boldsymbol{v}_S|$ indicates the direction of sliding between the two particles, where the slip velocity $\boldsymbol{v}_S$ is defined by $\boldsymbol{v}_S = \boldsymbol{v}_R - (\boldsymbol{v}_R \cdot \boldsymbol{n})\boldsymbol{n} + r_i \boldsymbol{\Omega}_i \times \boldsymbol{n} + r_j \boldsymbol{\Omega}_j \times \boldsymbol{n}$ and $\boldsymbol{v}_R = \boldsymbol{v}_i - \boldsymbol{v}_j$ is the particle relative velocity. There is no adhesive force between the particles and no rolling resistance. The normal force F_n is composed of the elastic force F_{ne} and a dissipative force F_{nd}. The Hertz (1882) expression gives the elastic part of the normal force as

$$F_{ne} = -k_N \delta_N = -K \delta_N^{3/2}, \tag{3.6}$$

where $K = (4/3)E\sqrt{R}$ and $\delta_N = r_i + r_j - |\boldsymbol{x}_i - \boldsymbol{x}_j|$ is the particle overlap. The particle effective radius and elastic modulus, R and E, are defined by

$$\frac{1}{R} \equiv \frac{1}{r_i} + \frac{1}{r_j}, \quad \frac{1}{E} \equiv \frac{1-\sigma_i^2}{E_i} + \frac{1-\sigma_j^2}{E_j}, \tag{3.7}$$

where σ_i and σ_j are the Poisson ratios, and E_i and E_j are the elastic moduli of the individual particles. The dissipation force F_{nd} is given by

$$F_{nd} = -\eta_N \, \boldsymbol{v}_R \cdot \boldsymbol{n}, \tag{3.8}$$

where η_N is the normal friction coefficient. Tsuji, Tanaka & Ishida (1992) propose an expression for η_N of the form

$$\eta_N = \alpha \, (m k_N)^{1/2}, \tag{3.9}$$

where the coefficient α is written as a function of the coefficient of restitution e. In the current paper, the Stokes number is sufficiently small that we set $e = 0$, in accordance with the experimental results of Joseph *et al.* (2001).

We use a spring–dashpot–slider model for the sliding resistance proposed by Cundall & Strack (1979), in which the tangential sliding force F_s is first absorbed by the spring and dashpot until its magnitude reaches a critical value $F_{crit} = \mu_f |F_n|$. A rotational form of the spring–dashpot model is used for the twisting resistance (Marshall 2009*b*). Since small particles tend not to slip very much upon collision, we

Case	ε	St	Re_F	$Re_{p,nom}$	A	c_0
A	0.12	0.008	10	0.01	0.2	0.005
B	0.02	0.002	100	0.004	0.2	0.0006
C	0.02	0.002	100	0.004	0.1	0.0006

TABLE 1. Parameter values for DEM simulations, including the dimensionless particle diameter, the Stokes number, the flow Reynolds number, the nominal particle Reynolds number, the dimensionless corrugation-wave amplitude and the nominal particle concentration. All cases reported are for neutrally buoyant particles ($\chi = 1$) with corrugation wavelength $\lambda = 2$.

refer to our previous papers (Marshall 2006; Marshall 2009*b*) for details of the slip and twisting resistance forces and torques.

4. Particle focusing at moderate Reynolds number ($Re_F = 10$)

The DEM calculations are initialized by placing particles in an array in the tube with random initial velocities. A preliminary calculation is then performed with no flow in the tube and no fluid drag on the particles, during which time the particles are allowed to bounce around within the tube until they achieve a state in which the concentration profile is essentially uniform. In some cases, the initialization is performed within the entire corrugated tube, while in other cases, where we wish to focus on the particle transport within the central portion of the tube, the initialization is performed for a tube of constant radius with value less than the minimum wall position of the corrugated tube. The results of this preliminary calculation are then used as the initial condition for the DEM simulations with the corrugated tube.

A listing of parameters used for all DEM calculations is given in table 1. In addition to the flow Reynolds number and the Stokes number, we list a nominal particle Reynolds number $Re_{p,nom} = St\, \varepsilon Re_F$. The instantaneous particle Reynolds number $Re_p = |\boldsymbol{v} - \boldsymbol{u}|d/\nu$ will vary with time for each particle depending on the current value of the relative velocity. The nominal particle Reynolds number gives a value that is characteristic of the particles in the flow based on the estimate $|\boldsymbol{v} - \boldsymbol{u}| = O(St\, U)$ for the relative velocity at low Stokes number (Crowe *et al.* 1998). For all cases, the nominal particle Reynolds number is very small.

Results of a DEM simulation for a case with $Re = 10$ are shown in figure 6 for case A in table 1. The particle diameter in this computation ($\varepsilon = 0.12$) is chosen to be fairly large in order to yield a sufficiently large value of the Stokes number ($St = 0.008$) that particle focusing will be observed over the computational period. The corrugation-wave amplitude ($A = 0.2$) is selected to be fairly large for the same reason. The particles are plotted in an end view, looking down the end of the tube, at the initial time, at an intermediate time ($t = 25$) and at a much later time ($t = 400$) after which the particles have achieved a state of statistical equilibrium. The nominal dimensionless time for a particle to pass one furrow length is equal to the wavelength ($\lambda = 2$). A solid circle and a dashed circle are used in figures 6(*a*)–6(*c*) to indicate the innermost and outermost values of the tube radii, respectively, corresponding to the trough ($r = 0.8$) and crest ($r = 1.2$) radii of the wall corrugations. For this particular simulation, the particles are initialized within a uniform tube of radius $r = 0.8$ so as to concentrate on the transport within the central part of the tube.

It is observed in figure 6 that the particles steadily drift towards the centre of the tube. The particles close to the $r = 0.8$ initialization radius contract quickly down to

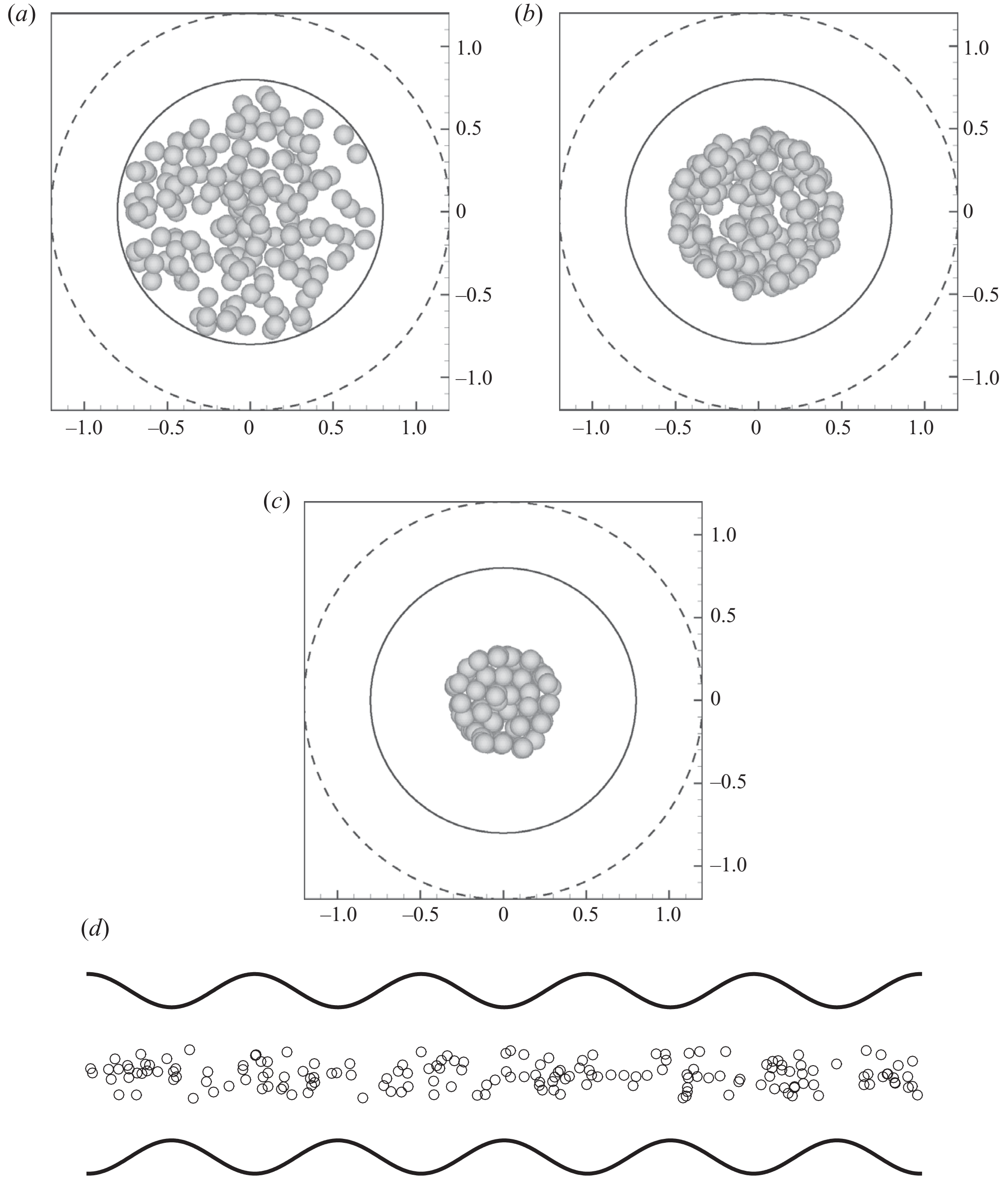

FIGURE 6. Time series showing inward particle drift for case A at times (*a*) $t = 0$, (*b*) $t = 25$ and (*c*) $t = 400$. The dashed and solid lines represent the maximum and minimum locations of the tube surface, corresponding to the wave crest and trough, respectively. (*d*) A side view of (*c*) the end configuration.

a radius just less than $r = 0.5$. It takes nearly 12 times longer for the particles to then contract within a radius $r = 0.25$ of the tube centre. The slow contraction as the particles become more dense near the centre of the tube is primarily caused by the radial variation in the particle drift velocity, but more frequent collisions also play a role in mitigating the particle inward drift at large times. We note that the end-view images in figure 6 make the particles appear much more concentrated than is actually the case. In a side view, as seen in figure 6(*d*), it is apparent that the particles are

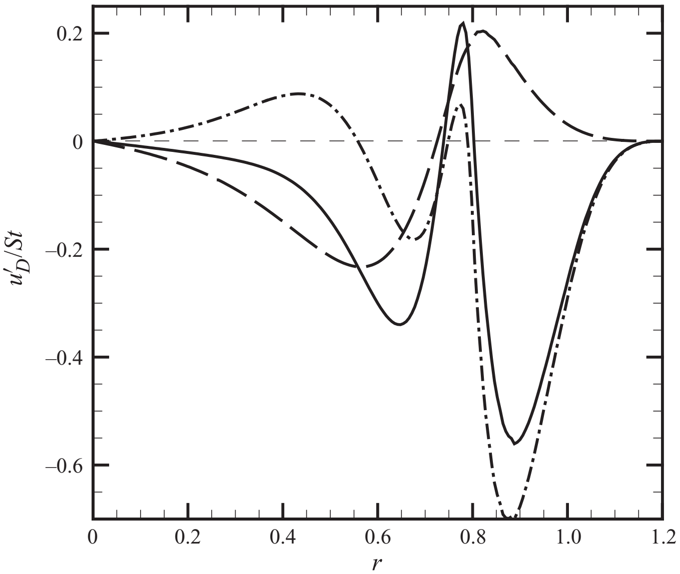

FIGURE 7. First drift velocity u'_{D1} (long dashed line), second drift velocity u'_{D2} (dashed–dotted line) and sum $u'_{D1} + u'_{D2}$ (solid line) normalized by St for case A.

spread out in a fairly low-concentration suspension along the tube axis, so that the collisions are relatively infrequent.

A plot showing the radial variation of the first and second drift velocities, u_{D1} and u_{D2}, defined by (2.11), and the sum $u_{D1}+u_{D2}$ is given for this flow in figure 7, where we divide the drift velocities by the Stokes number. We note that the corrugation-wave amplitude for this case ($A = 0.2$) only marginally satisfies the requirement of small amplitude required for the validity of the expansion (2.10). As was also observed for the flow under the lubrication theory, the first drift velocity dominates within the inner part of the tube, leading to a net inward drift of the particles. The two drift velocities change sign in the middle region of the tube and the magnitude of the second drift velocity increases until it is greater than the first drift velocity. The net result is that the sum $u_{D1} + u_{D2}$ exhibits two negative peaks: one in the inner part of the tube and the other in the outer region of the tube. In-between, there is a region within the interval $0.7 < r < 0.8$ in which the net drift velocity changes sign to become positive, indicating an outward drift. However, no indication of outward drift is observed in the DEM computations for this case. The difference is likely due to the neglect of higher order terms in η in the Taylor-series expression (2.10). We also observe that there is a large radial variation in the total drift magnitude. For instance, the value of the total drift velocity at $r = 0.65$ is nearly 10 times larger than that at $r = 0.2$. This large radial variation in drift velocity is the primary reason why the rate of particle focusing slows down as particles approach the centre of the tube.

Figure 8 illustrates the effect on the first and second drift velocity terms as the wave amplitude and wavelength are varied. The effect of wavelength can be examined by comparing the two plots shown in figures 8(*a*) and 8(*b*), which are given for cases with $\lambda = 1$ and 2, respectively. The overall form of the drift-velocity variation in the two cases is similar. However, the case with smaller wavelength exhibits higher peak values of drift-velocity magnitude, while the drift velocity within the centre region of the tube ($r < 0.5$) is smaller than for the case with longer wavelength. It is therefore

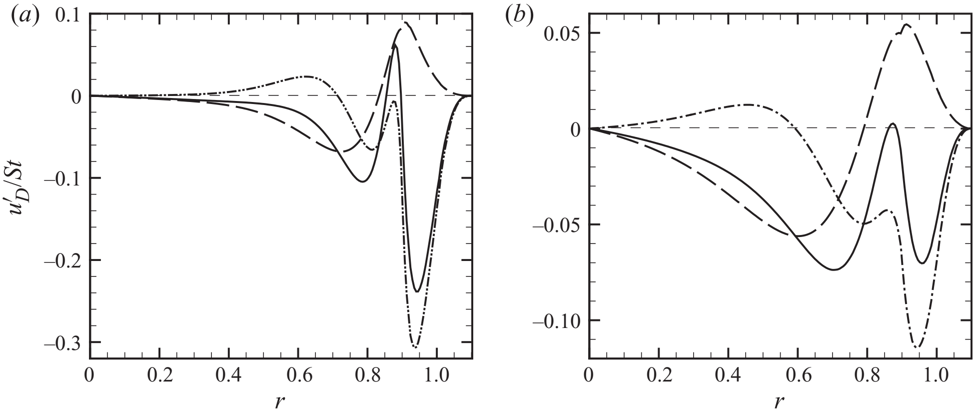

FIGURE 8. Plots showing the effect of wavelength and amplitude on the first and second particle drift velocities, using the same line definitions as in figure 7. Cases are shown for $Re_F = 10$ and (*a*) $\lambda = 1$ and $A = 0.1$ and (*b*) $\lambda = 2$ and $A = 0.1$.

expected that as wavelength decreases, particles will drift inwards more quickly from the outer regions of the tube, but then take a longer time to focus once they are in the central part of the tube. It is also noted that, like the case shown in figure 7, the small-wavelength case exhibits a region of positive total drift velocity within the interval $0.8 < r < 0.9$, suggesting that particles initialized in the outer part of the tube experience a barrier in passing into the central tube region. The effect of corrugation-wave amplitude can be examined by comparing figures 7 and 8(*b*), both of which have a wavelength of $\lambda = 2$, but different amplitudes. It is apparent that an increase in amplitude drastically increases the magnitude of the drift velocity. For instance, the peak in the negative total drift velocity occurring near $r = 0.65$ is about 4.5 times larger for the $A = 0.2$ case than it is for the $A = 0.1$ case.

5. Particle focusing at higher Reynolds number ($Re_F = 100$)

The effect of the flow Reynolds number was explored for a fixed tube geometry with $A = 0.1$ and $\lambda = 2$, corresponding to the non-recirculating-flow case shown in figure 2. The furrow-averaged radial acceleration $\bar{a}_r(\bar{r})$, which is proportional to the negative of the first drift velocity, is plotted in figure 9 for cases with flow Reynolds numbers of 1, 10 and 100, as well as the lubrication-theory solution (2.12a), which is essentially a zero-Reynolds-number solution. Consistent with our theoretical derivation, the lubrication-theory result is truncated at $r = 1$, since the waves on the tube are assumed to be small. We note that the $\bar{a}_r(\bar{r})$ term dominates the inward drift velocity in the centre region of the tube, as discussed in the previous section, and hence the plot in figure 9 gives an indication of the influence of the flow Reynolds number on the rate of inward particle drift. While all curves in figure 9 have the same basic form, the value of $\bar{a}_r(\bar{r})$ is observed to decrease markedly with increase in the flow Reynolds number for a given tube geometry. For instance, the maximum positive value of $\bar{a}_r(\bar{r})$ is 0.2 for the lubrication theory ($Re_F = 0$), but it is only 0.02 for the case with $Re_F = 100$.

Results of a DEM simulation for a case with $Re_F = 100$ and $A = 0.2$ (case B) are given in figure 10, again showing an end view looking down the tube. Dashed and solid lines represent the maximum and minimum locations of the tube surface

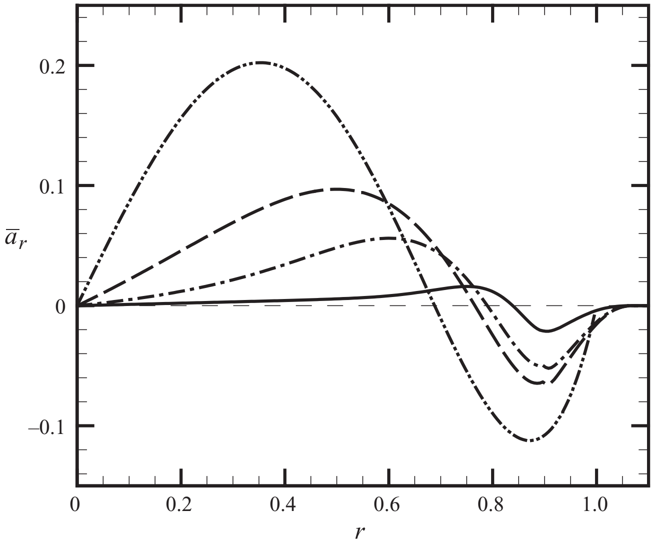

FIGURE 9. Plots showing the effect of the Reynolds number on the furrow-averaged radial acceleration (evaluated at a fixed radial location) for cases with $A = 0.1$ and $\lambda = 2$, and flow Reynolds numbers of 100 (solid line), 10 (dashed–dotted line), 1 (dashed line) and the lubrication-theory solution (dashed–double-dotted line).

waves. Particles are initialized within a tube of radius $r = 0.8$, with approximately uniform concentration profile, using the same initialization procedure as described in § 4, for particles with diameter $\varepsilon = 0.02$. The particles within the outer part of the tube are initially observed to contract quickly inwards towards the tube centre, as was observed for the $Re_F = 10$ flows. However, at a radius of about $r = 0.55$, the inward motion of these particles slows to such an extent that little further motion is discernable in the computations. Particles at radial positions between the tube centre and a radius of $r = 0.55$ are observed to advect down the tube with little observable net radial movement within the computational time period. Since the particle field is fairly axisymmetric, we can quantify the particle inward drift in time using a radial-concentration profile. For instance, for the case shown in figure 10, the corresponding concentration profiles are plotted in figure 11. The concentration is initially nearly uniform across the tube. By $t = 50$, the outermost particles have drifted inwards to form a concentration peak at about $r = 0.6$, but there has been little change in the concentration within the inner region of the tube. At times $t = 600$ and $t = 1900$, a sharp peak of particle concentration is observed at $r = 0.55$, with no significant change in concentration between these two times.

The first and second drift velocities, normalized by the Stokes number, for the case shown in figure 10 are plotted in figure 12, along with the total drift velocity. The second drift velocity exhibits large peaks for cases with flow recirculation in the outer part of the tube; so the plot in figure 12 focuses on the inner tube region $r < 0.7$. As noted previously in this section, the magnitude of both of the drift velocities in the region close to the tube centre is much smaller for the $Re_F = 100$ case than it is for cases with lower Reynolds number. The total drift velocity is observed to be negative throughout the central region of the tube ($r < 0.5$), but to have a very small magnitude, which is consistent with the negligible motion of the particles within the centre part of the tube observed in the DEM simulation.

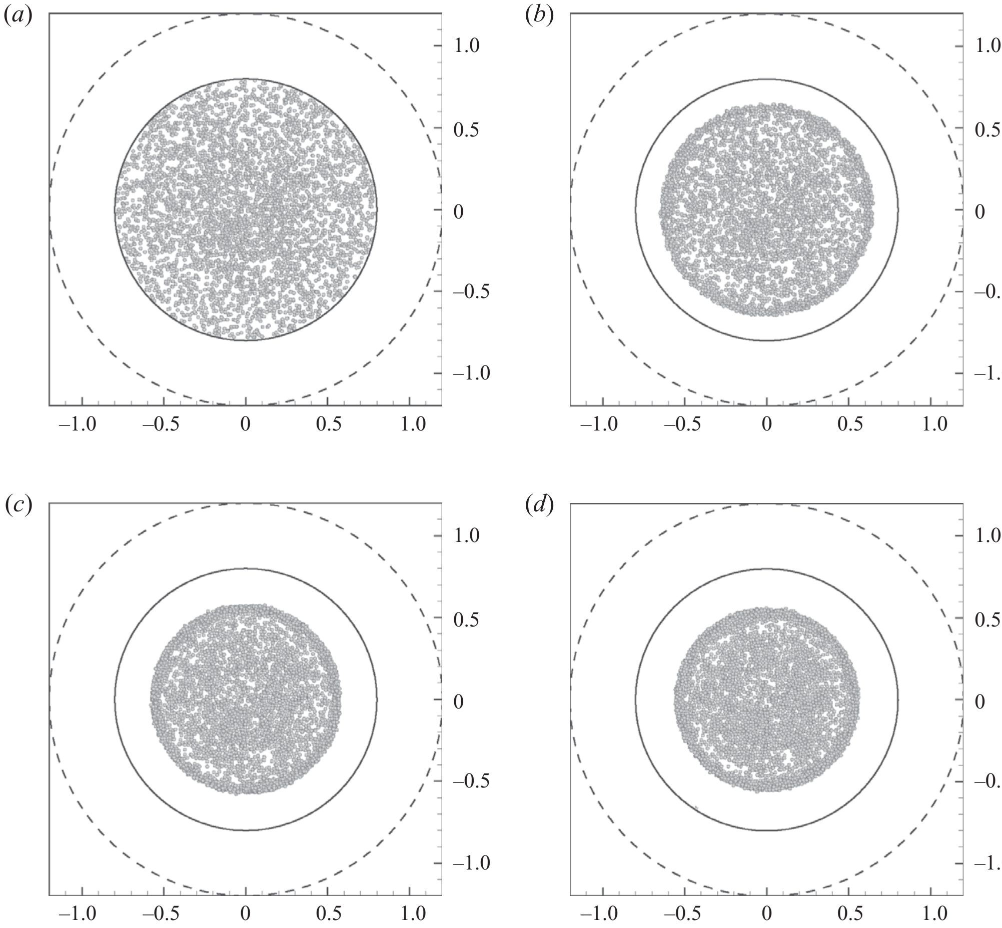

FIGURE 10. Time series showing formation of a particle ring for case B at times (*a*) $t = 0$, (*b*) $t = 50$, (*c*) $t = 600$ and (*d*) $t = 1900$. The dashed and solid lines represent the maximum and minimum locations of the tube surface, corresponding to the wave crest and trough, respectively.

In order to examine the effect of corrugation amplitude on the particle-ring formation, the computation described in figures 10 and 11 was repeated with a smaller amplitude of $A = 0.1$ (case C). The concentration profiles for this case are shown in figure 13 at the same four times as shown in figure 11. The particles in the outer region of the tube exhibit the same tendency drift into a ring as observed for the $A = 0.2$ case, but the rate of ring formation is substantially slower. This result is consistent with the observation from the previous section for $Re = 10$ that the particle drift velocity increases with increase in corrugation amplitude.

The transport of particles within the outer part of the tube is examined by repeating the computation shown in figures 10 and 11 for a case where particles are initialized everywhere within the corrugated tube, with an approximately uniform concentration distribution. It is observed that most of the particles within the outer region drift inwards to collect in the particle ring, as shown in figure 10. However, some particles become trapped in the recirculating-flow regions within the furrows, and eventually become trapped by the flow field against the tube wall. A plot of the fluid streamlines

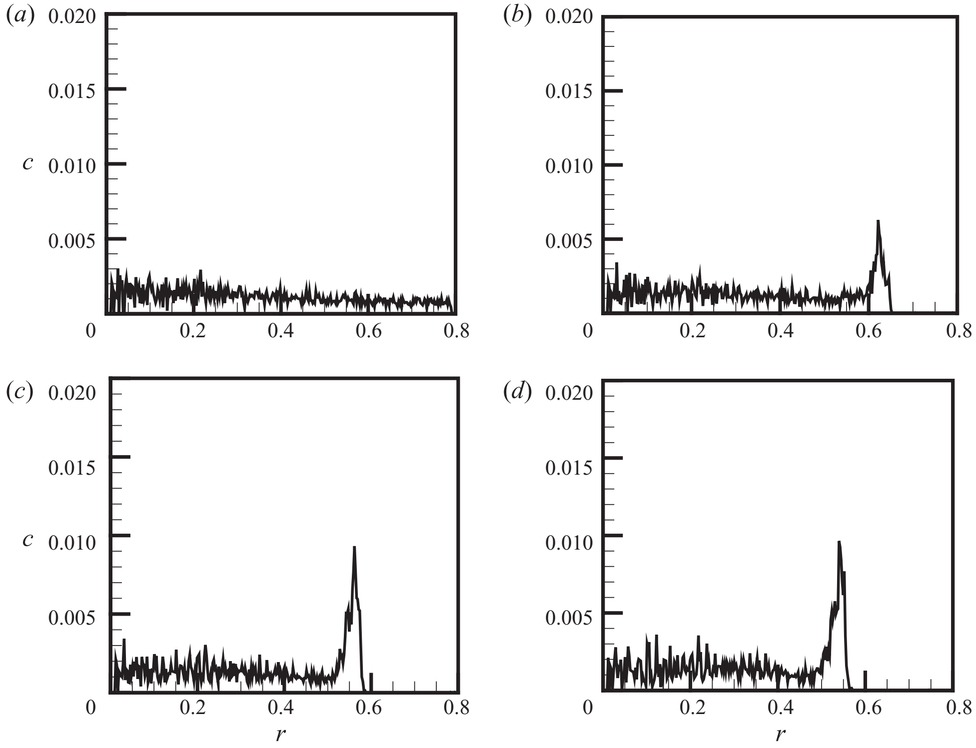

FIGURE 11. Concentration profiles for the case shown in figure 10, at the same four times.

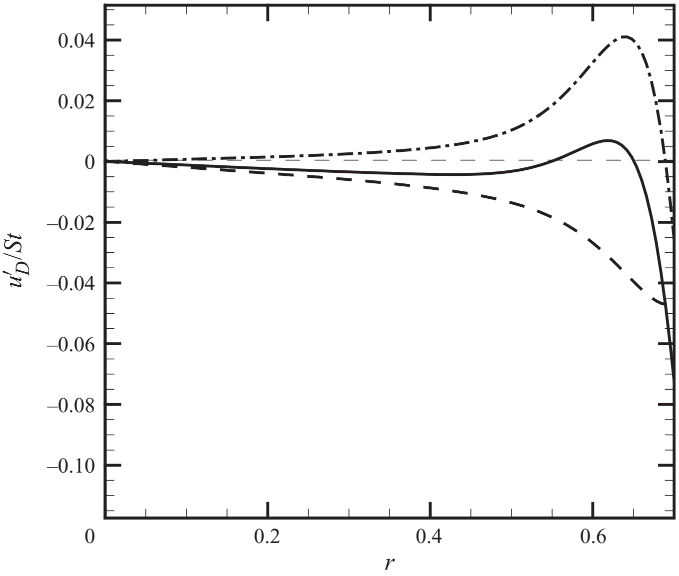

FIGURE 12. First drift velocity u'_{D1} (long dashed line), second drift velocity u'_{D2} (dashed–dotted line) and sum $u'_{D1} + u'_{D2}$ (solid line) normalized by St for case B.

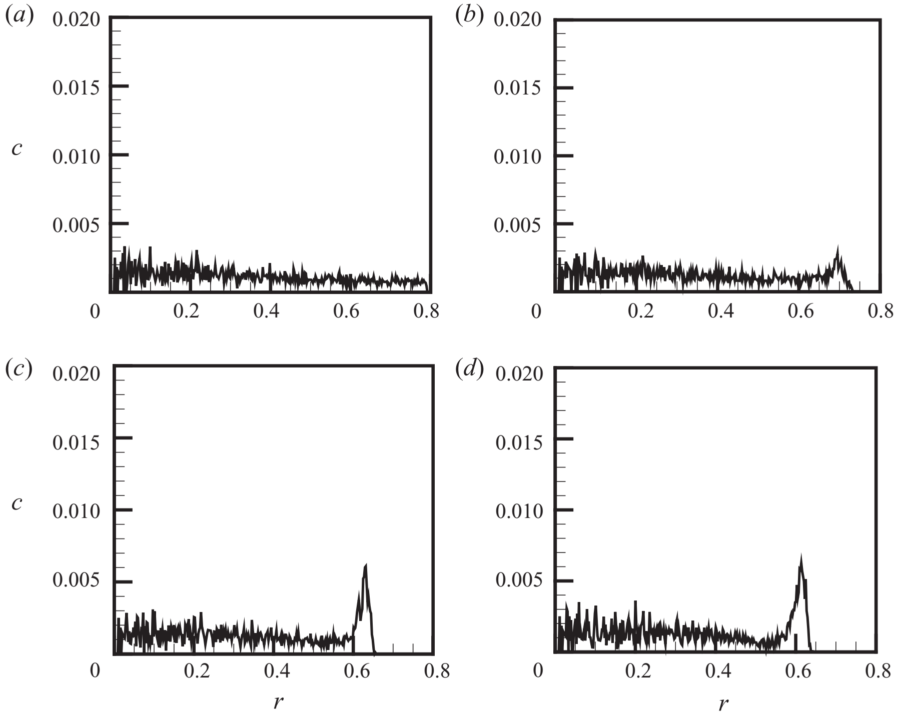

FIGURE 13. Concentration plots for case C at times (*a*) $t = 0$, (*b*) $t = 50$, (*c*) $t = 600$ and (*d*) $t = 1900$. Convergence to a particle ring is much slower than for the case shown in figure 11.

within one furrow is shown in figure 14(*a*), with a close-up schematic showing the location in which particles become trapped given in figure 14(*b*) (for the region indicated by a rectangle in figure 14*a*). A stagnation point exists at the wall between the recirculation region and the bulk flow, near which particles tend to collect. Since no adhesion force acts between the particles, this trapping effect is purely hydrodynamic.

The focusing effect exhibited by each of the cases examined is summarized in figure 15, in which the root-mean-squared radial position of the particles is plotted as a function of the nominal number of furrows traversed. It is apparent that the $Re_F = 10$ case focuses the particles much more quickly than do the cases with $Re_F = 100$, which is consistent with the rapid decrease in the first drift velocity with the Reynolds number shown in figure 9. Comparing the two $Re_F = 100$ cases, doubling of the corrugation amplitude is observed to increase the particle-focusing rate by a factor of approximately 4, as predicted by the lubrication-theory expressions (2.12*a*,*b*). All cases exhibit a relatively rapid initial focusing within the first 200 furrows traversed, followed by much slower further focusing. This observation suggests that it might be beneficial, in practice, to design a device in which extraction of the particle-rich fluid at the centre of the tube is repeated at regular intervals along the tube length, rather than only at the end of the corrugated tube section.

It is noted that despite certain superficial similarities, the physical process driving the particle-focusing phenomenon reported in the current study is entirely different from particle migration that is sometimes observed in straight tubes, such as the Segre–Silberberg effect (Segre & Silberberg 1962) or the effects of shear-induced migration caused by particle collisions (Leighton & Acrivos 1987). The

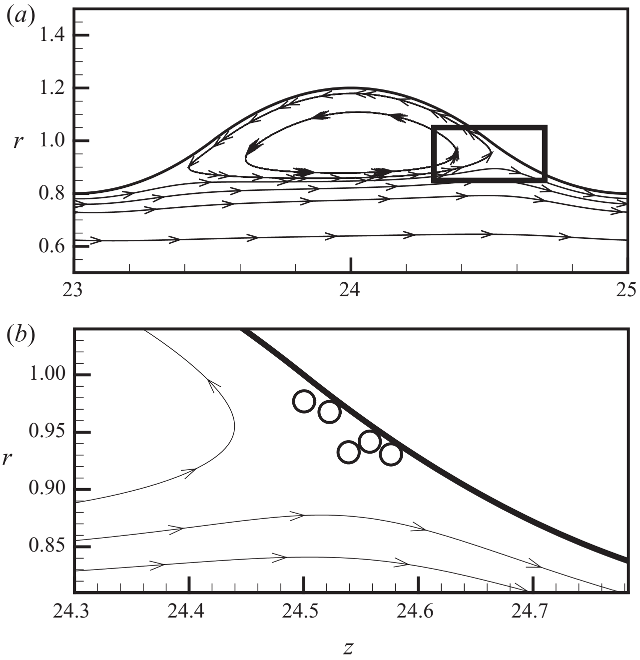

FIGURE 14. Schematic of particles initialized within the furrows being caught on the downstream constriction for case B. The close-up in (*b*) shows the locations of particles caught on the outer tube surface within the insert region in (*a*) (indicated by a rectangle).

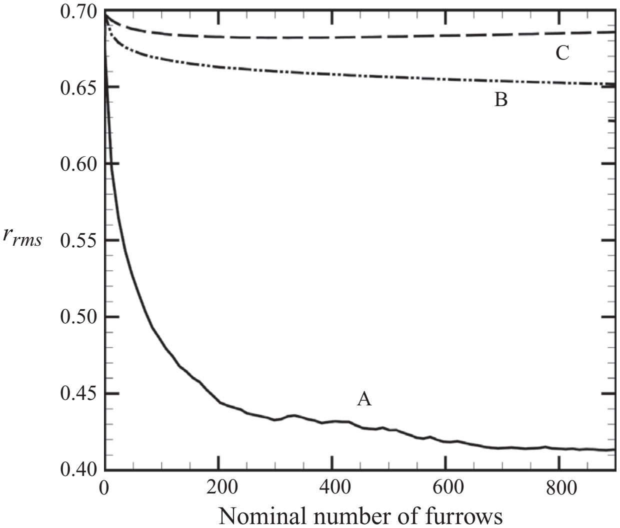

FIGURE 15. Root-mean-square particle radius as a function of nominal number of furrows traversed for case A (solid line), case B (dashed–double-dotted line) and case C (dashed line).

Segre–Silberburg effect, in which particles are observed to migrate to a radius of about 0.6 times the tube radius, occurs due to inertial effects in the flow about the particles (Ho & Leal 1974). While inertia is always present to some extent, experimental results by Han *et al.* (1999) indicate that this effect is so slow as to often not be discernable for the particle Reynolds numbers below about 0.2. Shear-induced migration due to particle collisions causes particles to drift to the low-shear region near the tube centre. However, experimental results by Hampton *et al.* (1997) and others at low particle Reynolds numbers show that shear-induced diffusion has negligible influence at particle concentrations of 10 % or less. For the present study, the particle concentration is 0.5 % or lower and the particle Reynolds number is 0.01 or lower for all cases. We have repeated a number of the computations reported in this study for a straight tube and have not been able to identify any particle migration, which is in agreement with findings from the literature cited above for the flow at low concentrations and particle Reynolds numbers.

6. Conclusions

Focusing of particles in a suspension flow down a corrugated axisymmetric tube has been investigated in this paper. At low flow Reynolds numbers, the particles are observed to drift towards the centre of the tube at a rate that is proportional to the Stokes number and the square of the tube maximum corrugation-wave slope. The particle drift is governed by the sum of two competing drift velocities, one of which is proportional to the axial average of the fluid radial acceleration and the other of which is proportional to the average of the particle radial deviation from its averaged position times the gradient of the fluid radial acceleration. The first of these drift velocities tends to move particles inwards within the inner part of the tube and outwards within the outer part of the tube, whereas the second drift velocity tends to do the opposite. The rate of particle drift is observed to increase markedly with increase in the amplitude of the tube-wall corrugations, but it decreases with increase in the flow Reynolds number. Computations are performed for flow Reynolds numbers of 10 and 100 using a DEM. Consistent with the theoretical estimates for drift velocities, the computations indicate particles drifting inwards and collecting at the tube centre for the $Re_F = 10$ case. For the $Re_F = 100$ case, particles in the outermost regions of the tube drift inwards to form a ring of relatively higher concentration at a radius of about 55 % of the tube nominal radius. Particles within the inner part of the tube exhibit almost no net drift for this high-Reynolds-number case.

The phenomenon reported in the current paper is shown to be distinct from the well-known Segre–Silberberg effect or other types of particle migration observed for straight tubes. Specifically, the particle focusing discussed in this paper is not observed in flows with straight tubes at the low values of the particle Reynolds number and the particle concentration used in these computations. The observation from the lubrication-theory solution that the rate of particle focusing is proportional to the square of the corrugation-wave amplitude is observed to approximately hold in finite-volume/DEM simulations at higher flow Reynolds number (e.g. $Re_F = 100$).

The particle-focusing phenomenon reported in this paper might be of use for separation of particles from a suspension by passage of the suspension down a corrugated tube. Such a device might be of use, for instance, in separation of algae from a suspension or in the particle and cell separation problems that arise in microfluidic assay systems. However, to be effective, the tube flow would need to be confined to low Reynolds numbers and the section of the tube would need to be sufficiently long to allow the particle focusing to develop. The lubrication theory developed in § 2 can be used to obtain an estimate for the required tube length under different conditions, but it should be noted that the particle focusing developed with the lubrication theory is a best-case (zero-Reynolds-number) scenario. As demonstrated in this paper, the rate of particle focusing is significantly slowed at finite Reynolds numbers.

This study was supported by the US Department of Transportation (grant number DTOS59-06-G-00048) and by Vermont EPSCoR (grant number EPS 0701410).

Appendix

The radial particle drift can be approximated to a leading order in the Stokes number by (2.8), such that

$$u_D \cong -St\frac{\mathrm{D}u'}{\mathrm{D}t'} = -St\left(\frac{\partial u'}{\partial t'} + u'\frac{\partial u'}{\partial r'} + w'\frac{\partial u'}{\partial z'}\right). \tag{A 1}$$

Substituting (2.5) for u' and w' into (A 1) and retaining terms through second order in η, with $h' = 1 + \eta\cos(\alpha z')$, gives

$$u' = -2\alpha\eta\, r'[1 - 3\eta\cos(\alpha z')]\sin(\alpha z') + 2\alpha\eta\, r'^3[1 - 5\eta\cos(\alpha z')]\sin(\alpha z'), \tag{A 2a}$$

$$w' = 2\left\{1 - r'^2[1 - 2\eta\cos(\alpha z') + 3\eta^2\cos^2(\alpha z')]\right\}[1 - 2\eta\cos(\alpha z') + 3\eta^2\cos^2(\alpha z')], \tag{A 2b}$$

$$\frac{\partial u'}{\partial r'} = -2\alpha\eta[1 - 3\eta\cos(\alpha z')]\sin(\alpha z') + 6r'^2\alpha\eta[1 - 5\eta\cos(\alpha z')]\sin(\alpha z'), \tag{A 2c}$$

$$\begin{aligned}\frac{\partial u'}{\partial z'} &= -2(\alpha\eta)^2 r'(3 - 5r'^2)\sin^2(\alpha z') - 2\alpha^2\eta\, r'[1 - 3\eta\cos(\alpha z')]\cos(\alpha z')\\ &\quad + 2\alpha^2\eta\, r'^3[1 - 5\eta\cos(\alpha z')]\cos(\alpha z').\end{aligned} \tag{A 2d}$$

Computing the furrow average (2.9) of the radial convective acceleration terms from (A 1) gives

$$\overline{u'\frac{\partial u'}{\partial r'}} = 2(\alpha\eta)^2 r'(1 - r4'^2 + 3r'^4), \quad \overline{w'\frac{\partial u'}{\partial z'}} = 2(\alpha\eta)^2 r'(2 - 6r'^2 + 4r'^4). \tag{A 3}$$

Summing these two terms and substituting into the first equation in (2.11) yields the expression (2.12*a*) for the first drift velocity.

The second drift-velocity term contains two parts – a radial-position displacement and a radial-acceleration gradient – both of which are $O(\eta)$. The radial-position displacement is obtained by substituting (A 2*a*) and (A 2*b*) for u' and w' into $r' - \bar{r}' = \int (u'/w')\,\mathrm{d}z'$, performing the integration over z', and retaining only terms of $O(\eta)$ to yield

$$r' - \bar{r}' = \eta r'\cos(\alpha z'). \tag{A 4}$$

The radial acceleration gradient is obtained by differentiating the two convective acceleration terms in (A 1) to get

$$\frac{\partial a'}{\partial r'} = \left(\frac{\partial u'}{\partial r'}\right)^2 + u'\frac{\partial^2 u'}{\partial r'^2} + \frac{\partial w'}{\partial r'}\frac{\partial u'}{\partial z'} + w'\frac{\partial^2 u'}{\partial r'\partial z'}. \tag{A 5}$$

The first two terms on the right-hand side of (A 5) are $O(\eta)^2$ and are therefore negligible. Retaining only the $O(\eta)$ parts of the third and fourth terms yields

$$\frac{\partial a'}{\partial r'} = -4\alpha^2 \eta (1 - r'^2)(1 - 5r'^2)\cos(\alpha z'). \tag{A 6}$$

Substituting (A 4) and (A 6) into the second equation in (2.11) and performing the furrow average operation (2.9) yields the expression (2.12*b*) for the second particle drift velocity.

REFERENCES

AMON, C. H., GUZMÁN, A. M. & MOREL, M. B. 1996 Lagrangian chaos, Eulerian chaos, and mixing enhancement in converging–diverging channel flows. *Phys. Fluids* **8**, 1192–1206.

ASAKO, Y. & FAGHRI, M. 1987 Finite volume solutions for laminar flow and heat transfer in a corrugated duct. *J. Heat Transfer* **109**, 627–634.

ASAI, M. & FLORYAN, J. M. 2006 Experiments on the linear instability of flow in a wavy channel. *Eur. J. Mech.* B/*Fluids* **25**, 971–986.

CABAL, A., SZUMBARSKI, J. & FLORYAN, J. M. 2002 Stability of flow in a wavy channel. *J. Fluid Mech.* **457**, 191–212.

CHO, K. J., KIM, M. & SHIN, H. D. 1998 Linear stability of two-dimensional steady flow in wavy-walled channel. *Fluid Dyn. Res.* **23**, 349–370.

CHOI, S. & PARK, J.-K. 2008 Sheathless hydrophoretic particle focusing in a microchannel with exponentially increasing obstacle arrays. *Anal. Chem.* **80**, 3035–3039.

CHOI, S., SONG, S., CHOI, C. & PARK, J.-K. 2008 Sheathless focusing of microbeads and blood cells based on hydrophoresis. *Small* **4** (5), 634–641.

CHRISTI, Y. 2007 Biodiesel from microalgae. *Biotechnol. Adv.* **25**, 294–306.

CROWE, C., SOMMERFELD, M. & TSUJI, Y. 1998 *Multiphase Flows with Droplets and Particles*, pp. 24–32. CRC Press.

CUNDALL, P. A. & STRACK, O. D. L. 1979 A discrete numerical model for granular assembles. *Geotechnique* **29** (1), 47–65.

DAVIS, J. A., INGLIS, D. W., MORTON, K. J., LAWRENCE, D. A., HUANG, L. R., CHOU, S. Y., STURM, J. C. & AUSTIN, R. H. 2006 Deterministic hydrodynamics: taking blood apart. *Proc. Natl. Acad. Sci. USA* **103**, 14779–14784.

DI CARLO, D., IRIMIA, D., TOMPKINS, R. G. & TONER, M. 2007 Continuous inertial focusing, ordering and separation of particles in microchannels. *Proc. Natl. Acad. Sci. USA* **104** (48), 18892–18897.

DI FELICE, R. 1994 The voidage function for fluid–particle interaction systems. *Intl J. Multiph. Flow* **20**, 153–159.

FERRY, J. & BALACHANDAR, S. 2003 A locally implicit improvement of the equilibrium Eulerian method. *Intl J. Multiph. Flow* **29**, 869–891.

GRADECK, M., HOAREAU, B. & LEBOUCHÉ, M. 2005 Local analysis of heat transfer inside corrugated channel. *Intl J. Heat Mass Transfer* **48**, 1909–1915.

GSCHWIND, P., REGELE, A. & KOTTKE, V. 1995 Sinusoidal wavy channels with Taylor–Goertler vortices. *Exp. Thermal Fluid Sci.* **11**, 270–275.

GUZMÁN, A. M. & AMON, C. H. 1994 Transition to chaos in converging–diverging channel flows: Ruelle–Takens–Newhouse scenario. *Phys. Fluids* **6** (6), 1994–2002.

GUZMÁN, A. M. & AMON, C. H. 1996 Dynamical flow characterization of transitional and chaotic regimes in converging diverging channels. *J. Fluid Mech.* **321**, 25–57.

HAMPTON, R. E., MAMMOLI, A. A., GRAHAM, A. L., TETLOW, N. & ALTOBELLI, S. A. 1997 Migration of particles undergoing pressure-driven flow in a circular conduit. *J. Rheol.* **41**, 621–640.

HAN, M., KIM, C., KIM, M. & LEE, S. 1999 Particle migration in tube flow of suspensions. *J. Rheol.* **43** (5), 1157–1174.

HERTZ, H. 1882 Über die Berührung fester elastische Körper. *J. reine Angew. Math.* **92**, 156–171.

Ho, B. P. & Leal, L. G. 1974 Inertial migration of rigid spheres in two-dimensional unidirectional flows. *J. Fluid Mech.* **65**, 365–400.

Huang, L. R., Cox, E. C., Austin, R. H. & Sturm, J. C. 2004 Continuous particle separation through deterministic lateral displacement. *Science* **304**, 987–990.

Issa, R. 1985 Solution of the implicit discretized fluid flow equations by operator splitting. *J. Comput. Phys.* **62**, 40–65.

Joseph, G. G., Zenit, R., Hunt, M. L. & Rosenwinkel, A. M. 2001 Particle–wall collisions in a viscous fluid. *J. Fluid Mech.* **433**, 329–346.

Kim, S. K. 2001 An experimental study of developing and fully developed flows in a wavy channel by PIV. *KSME Intl J.* **15** (12), 1853–1859.

Lai, Y. G. 2000 Unstructured grid arbitrarily shaped element method for fluid flow simulation. *AIAA J.* **38** (12), 2246–2252.

Lee, B. S., Kang, I. S. & Lim, H. C. 1999 Chaotic mixing and mass transfer enhancement by pulsatile laminar flow in an axisymmetric wavy channel. *Intl J. Heat Mass Transfer* **42**, 2571–2581.

Leighton, D. & Acrivos, A. 1987 The shear-induced migration of particles in concentrated suspensions. *J. Fluid Mech.* **181**, 415–439.

Mahmud, S., Islam, A. K. M. S. & Mamun, M. A. H. 2002 Separation characteristics of fluid flow inside two parallel plates with wavy surface. *Intl J. Engng Sci.* **40**, 1495–1509.

Marshall, J. S. 2006 Effect of shear-induced migration on the expulsion of heavy particles from a vortex core. *Phys. Fluids* **18** (11), 113301-1–113301-12.

Marshall, J. S. 2007 Particle aggregation and capture by walls in a particulate aerosol channel flow. *J. Aerosol Sci.* **38**, 333–351.

Marshall, J. S. 2009*a* Particle clustering in periodically-forced straining flows. *J. Fluid Mech.* **624**, 69–100.

Marshall, J. S. 2009*b* Discrete-element modeling of particulate aerosol flows. *J. Comput. Phys.* **228**, 1541–1561.

Nieno, B. & Nobile, E. 2001 Numerical analysis of fluid flow and heat transfer in periodic wavy channels. *Intl J. Heat Fluid Flow* **22**, 156–167.

Nishimura, T., Arakawa, S., Murakami, S. & Kawamura, Y. 1989 Oscillatory viscous flow in symmetric wavy-walled channels. *Chem. Eng. Sci.* **44** (10), 2137–2148.

Nishimura, T. & Kawamura, Y. 1995 Three-dimensionality of oscillatory flow in a two-dimensional symmetric sinusoidal wavy-walled channel. *Exp. Thermal Fluid Sci.* **10**, 62–73.

Nishimura, T., Murakami, S., Arakawa, S. & Kawamura, Y. 1990 Flow observations and mass transfer characteristics in symmetrical wavy-walled channels at moderate Reynolds numbers for steady flow. *Intl J. Heat Mass Transfer* **33** (5), 835–845.

Ormerod, M. G. 1999 *Flow Cytometry*. Springer-Verlag.

Oviedo-Tolentino, F., Romero-Méndez, R., Hernántez-Guerrero, A. & Girón-Palomares, B. 2008 Experimental study of fluid flow in the entrance of a sinusoidal channel. *Intl J. Heat Fluid Flow* **29**, 1233–1239.

Putz, R. & Pabst, R. 2000 *Sobotta Atlas of Human Anatomy*, 13th edn., vol. 2. Lippincott, Williams and Wilkins.

Ralph, M. E. 1986 Oscillatory flows in wavy-walled tubes. *J. Fluid Mech.* **168**, 515–540.

Rubinow, S. I. & Keller, J. B. 1961 The transverse force on a spinning sphere moving in a viscous fluid. *J. Fluid Mech.* **11**, 447–459.

Rush, T. A., Newell, T. A. & Jacobi, A. M. 1999 An experimental study of flow and heat transfer in sinusoidal wavy passages. *Intl J. Heat Mass Transfer* **42**, 1541–1553.

Saffman, P. G. 1965 The lift on a small sphere in a slow shear flow. *J. Fluid Mech.* **22**, 385–400.

Saffman, P. G. 1968 Corrigendum to 'The lift force on a small sphere in a slow shear flow'. *J. Fluid Mech.* **31**, 624.

Sastre, R. R., Csögör, Z., Perner-Nochta, I., Fleck-Schneider, P. & Posten, C. 2007 Scale-down of microalgae cultivations in tubular photo-bioreactors – a conceptual approach. *J. Biotechnol.* **132**, 127–133.

Savvides, G. N. & Gerrard, J. H. 1984 Numerical analysis of the flow through a corrugated tube with the application to arterial prosthesis. *J. Fluid Mech.* **138**, 129–160.

Segre, G. & Silberberg, A. 1962 Behavior of macroscopic rigid spheres in Poiseuille flow. Part 2. Experimental results and interpretation. *J. Fluid Mech.* **14**, 136–157.

Selvarajan, S., Tulapurkara, E. G. & Ram, V. V. 1999 Stability characteristics of wavy walled channel flows. *Phys. Fluids* **11** (3), 579–589.

Sobey, I. J. 1980 On flow through furrowed channels. Part 1. Calculated flow patterns. *J. Fluid Mech.* **96** (1), 1–26.

Stephanoff, K. D., Sobey, I. J. & Bellhouse, B. J. 1980 On flow through furrowed channels. Part 2. Observed flow patterns. *J. Fluid Mech.* **96** (1), 27–32.

Tsuji, Y., Tanaka, T. & Ishida, T. 1992 Lagrangian numerical simulation of plug flow of cohesionless particles in a horizontal pipe. *Powder Technol.* **71**, 239–250.

Usha, R., Senthilkumar, S. & Tulapurkara, E. G. 2005 Stability characteristics of suspension flow through wavy-walled channels. *Acta Mech.* **176**, 1–26.

Vasudeviah, M. & Balamurugan, K. 2001 On forced convective heat transfer for a Stokes flow in a wavy channel. *Intl Commun. Heat Mass Transfer* **28** (2), 289–297.